Coexistent three-component and two-component Weyl phonons in TiS, ZrSe, and HfTe

Jiangxu Li,[1] Qing Xie,[1,2] Sami Ullah,[1,2] Ronghan Li,[1] Hui Ma,[1] Dianzhong Li,[1] Yiyi Li,[1] and Xing-Qiu Chen[1,*]

[1]*Shenyang National Laboratory for Materials Science, Institute of Metal Research, Chinese Academy of Sciences, School of Materials Science and Engineering, University of Science and Technology of China, 110016, Shenyang, China*

[2]*University of Chinese Academy of Sciences, Beijing, 100049, China*

(Received 22 November 2017; published 12 February 2018)

In analogy to various fermions of electrons in topological semimetals, topological mechanical states with two types of bosons, Dirac and Weyl bosons, were reported in some macroscopic systems of kHz frequency, and those with a type of doubly-Weyl phonons in atomic vibrational framework of THz frequency of solid crystals were recently predicted. Here, through first-principles calculations, we have reported that the phonon spectra of the WC-type TiS, ZrSe, and HfTe commonly host the unique triply degenerate nodal points (TDNPs) and single two-component Weyl points (WPs) in THz frequency. Quasiparticle excitations near TDNPs of phonons are three-component bosons, beyond the conventional and known classifications of Dirac, Weyl, and doubly-Weyl phonons. Moreover, we have found that both TiS and ZrSe have five pairs of type-I Weyl phonons and a pair of type-II Weyl phonons, whereas HfTe only has four pairs of type-I Weyl phonons. They carry nonzero topological charges. On the $(10\bar{1}0)$ crystal surfaces, we observe topological protected surface arc states connecting two WPs with opposite charges, which host modes that propagate nearly in one direction on the surface.

DOI: 10.1103/PhysRevB.97.054305

I. INTRODUCTIONS

Topological insulators [1–3] and topological semimetals [4–8] are one of the fast growing families in the frontier of material sciences and condensed matter physics due to their unique density of states, transport properties, and novel topological surface states as well as their potential for use in quantum computers, spintronics, and novel physics. It has been well known that topological semimetals highlight several main types of interesting fermions in crystal solids, such as three-dimensional (3D) Dirac cones [9–21], Weyl nodes [22–44], Dirac nodal lines [45–60], triply degenerate nodal points [61–70], and hourglass fermions [71] as well as even beyond [61]. In addition, their realization in crystal solids is also important because they provide the ways to study elementary particles, which were long-sought and predicted ones, in high-energy physics. Importantly, in similarity to various fermions of electrons, the exciting progresses of bosons (vibrational phonons) have also been predicted [72] or observed in the 3D momentum space of solid crystals with the topological vibrational states, such as Dirac, Weyl, and line-node phonons in photonic crystals only with macroscopic systems of kHz frequency [72–87] and, recently, theoretically predicted doubly-Weyl phonons in transition-metal monosilicides with atomic vibrations at THz frequency [88]. Most recently, we have even predicted highly unique Weyl nodal straight-line phonons, extending the whole Brillouin zone (BZ) along the one-way BZ boundary, in the famous high-temperature superconductor MgB_2 [89]. However, to date within the atomistic periodic lattice with THz frequency, no single Weyl phonon has been reported and almost no three-component triply degenerate nodal phonons have been discussed, although three-component fermions have been experimentally confirmed [68] and phononic three-component degenerate nodal points have been mentioned at the high-symmetry Γ point in the zone center of the lattice BZ of transition-metal monosilicides [88].

The three-component phonons would possibly occur in atomic solid crystals because threefold degeneracy can be protected by lattice symmetries, such as symmorphic rotation combined with mirror symmetries and nonsymmorphic symmetries, as what was already demonstrated to be triply degenerated points of electronic fermions in the solid crystals [61–68]. In addition to the importance of seeking the new type of three-component bosons, the topological phononic states will be extremely interesting because they could certainly enable materials to exhibit novel heat transfer, phonon scattering, and electron-phonon interactions, as well as other properties related with vibrational modes, such as thermodynamics. In the first, in similarity to topological properties of electrons, the topological effects of phonons can induce the one-way edge phonon states (the topologically protected boundary states). These states will conduct phonon with little or no scattering [82,85], highlighting possible applications for designing phononic circuits [90]. Utilizing the one-way edge phonon states an ideal phonon diode [90] with fully 100% efficiency becomes potential in a multiterminal transport system. In the second, different from that of electrons, as one of bosons, phonons are not limited by the Pauli exclusion principle. This fact demonstrates that the whole frequency zone of phonon spectrum can be physically probed. It was even theoretically demonstrated that the chiral phonons excited by polarized photons can be detected by a valley phonon Hall effect in monolayer hexagonal lattices [91]. Within this context, through first-principles calculations we report on the coexistence of the triply degenerate nodal points (TDNPs) and type-I and

*Corresponding author: xingqiu.chen@imr.ac.cn

type-II Weyl nodes (WPs) of phonons in three compounds of TiS, ZrSe, and HfTe. Interestingly, these three materials simultaneously still exhibit three-component fermions and two-component Weyl fermions from their electronic structures. The coexistence of three-component bosons, two-component Weyl bosons, three-component fermions, and two-component Weyl fermions provide attractive candidates to study the interplays between topological phonons and topological fermions in the same solid crystals.

II. METHODS

Within the framework of the density functional theory (DFT) [92,93] and the density functional perturbation theory (DFPT) [94], we have performed the calculations on the structural optimizations, the electronic band structures, the phonon calculations, and surface electronic band structures. Both DFT and DFPT calculations have been performed by employing the Vienna *ab initio* simulation package (VASP) [95–97], with the projector augmented wave (PAW) pseudopotentials [98,99] and the generalized gradient approximation (GGA) within the Perdew-Burke-Ernzerhof (PBE) exchange-correlation functional [100,101]. The adopted PAW-PBE pseudopotentials of all elements treat semicore valence electrons as valence electrons. A very accurate optimization of structural parameters has been calculated by minimizing the interionic forces below 0.0001 eV/Å . The cutoff energy for the expansion of the wave function into the plane waves was 500 eV. The Brillouin zone integrations were performed on the Monkhorst-Pack k meshes ($21 \times 21 \times 23$) and were sampled with a resolution of $2\pi \times 0.014\text{Å}^{-1}$. The band structures, either with or without the inclusion of spin-orbit coupling (SOC), have been performed by the Gaussian smearing method with a width of smearing at 0.01 eV. Furthermore, the tight-binding (TB) through Green's function methodology [102–104] was used to investigate the surface states. We have calculated the Hamiltonian of tight-binding (TB) approach through maximally-localized Wannier functions (MLWFs) [105,106] by using the Wannier90 code [107]. To calculate phonon dispersions, force constants are generated based on finite displacement method within the $4 \times 4 \times 4$ supercells using the VASP code and their dispersions have been further derived by Phononpy code [108]. We have also computed the phonon dispersions by including the SOC effect, which has been turned out to be no influence in them. Furthermore, the force constants are used as the tight-binding parameters to build the dynamic matrices. We determine the topological charges of all WPs by using the Wilson-loop method [109,110]. The surface phonon DOSs are obtained by using the iteration Green's function method [104].

III. RESULTS

A. Crystal structure and structural stabilities of the *MX* compounds

Recently, the type of WC-type materials [Fig. 1(a)], including ZrTe, TaN, MoP, and WC, has been theoretically reported to host the coexistence of TDNPs and WPs in their electronic structures. This type of coexisted fermions of electronic TDNPs and WPs has been recently confirmed in

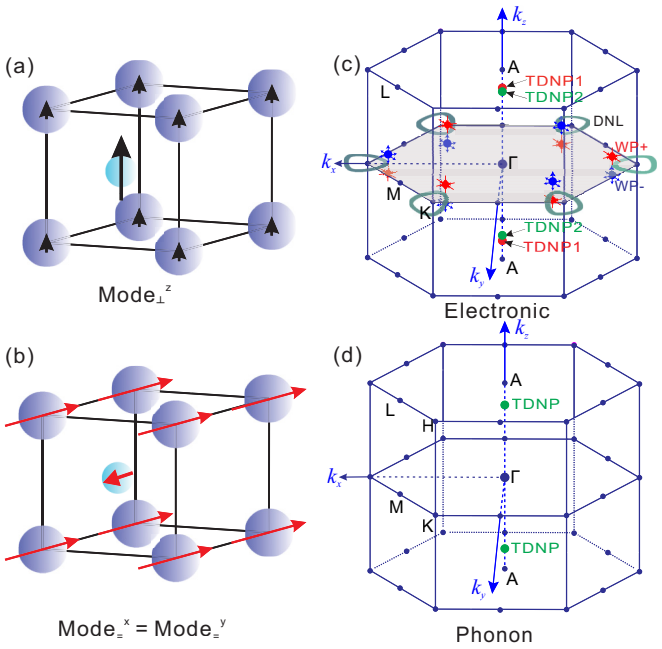

FIG. 1. WC-type crystal structure and its Brillioun zone of MX(M = Ti, Zr, Hf; X = S, Se, Te). These materials crystallize in the simple hexagonal crystal structure with the space group of $P\bar{6}m2$ (No. 187). M occupies the $1a$ Wyckoff site (0, 0, 0) and X locates at the $1d$ (1/3, 2/3, 1/2) site. Panel (a) shows the phonon vertical vibrational mode ($\text{Mode}^{z}_{\perp}$) along the k_z direction at the boundary—the high-symmetry A (0, 0, $\pi/2$) point—of the Brillioun zone (BZ). Panel (b) denotes the phonon planar vibrational mode ($\text{Mode}^{x}_{\parallel}$) along the k_x direction, which is twofold degenerate ($\text{Mode}^{x,y}_{\parallel} = \text{Mode}^{x}_{\parallel} = \text{Mode}^{y}_{\parallel}$) because of its C_{3v} rotational symmetry. (c) The BZ in which the closed loops around each K point denote the Dirac nodal lines (DNLs) of electrons around the Fermi level when SOC is ignored. With the SOC inclusion each DNL is broken into two Weyl points with the opposite chirality, marked as blue (WP-) and red (WP+) balls and they coexist with the triply degenerate nodal point (TDNP) of electronic structure (namely, three-component fermion). Panel (d) shows the triply degenerate nodal point (TDNP) of phonon dispersions (three-component boson) along the Γ-A direction in the BZ.

MoP [68]. We further extended this family by proposing eight compounds (TiS, TiSe, TiTe, ZrS, ZrSe, HfS, HfSe, and HfTe), which are isoelectronic and isostructural to ZrTe. Among these compounds, five compounds of TiS, ZrS, $ZrSe_{0.90}$, and $Hf_{0.92}Se$ as well as ZrTe were experimentally reported to have the same WC-type structure [111–118]. No experimental data is available for the remaining four compounds of TiSe, TiTe, HfS, and HfTe. Here, in order to systematically investigate their electronic structures and phonon spectra and to compare their differences, we have considered that all these nine compounds crystallize in the same WC-type structure. For five experimentally known compounds TiS, ZrS, ZrSe, ZrTe, and HfSe, our DFT calculations yield the good agreement of their equilibrium lattice parameters with the experimental data (see Supplemental Table S1 [119]). Their enthalpies of formation are derived in Supplemental Table S1 [119], indicating their stabilities in the thermodynamics and their phonon dispersions have no imaginary frequencies, revealing the stabilities in the atomic mechanical vibrations.

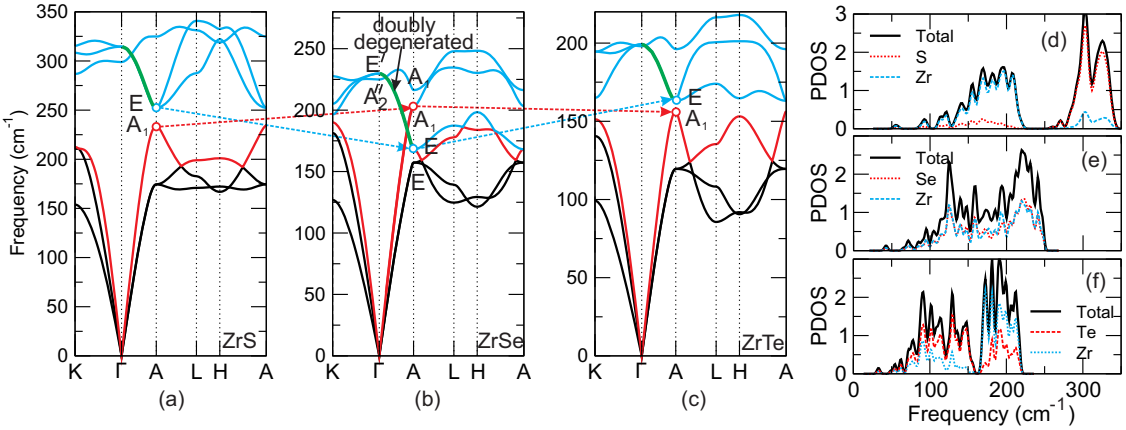

FIG. 2. Phonon spectra of ZrS, ZrSe, and ZrTe. Panels (a), (b), and (c): DFT-derived phonon dispersions of ZrS, ZrSe, and ZrTe, respectively. Panels (d), (e), and (f): DFT-derived total and partial phonon densities of states (PDOS) of ZrS, ZrSe, and ZrTe, respectively. At the high-symmetry A point, the symmetries of the modes are indicated by E, E, A_1, and A_1 with increasing frequencies and at the zone center (Γ) the symmetries of the modes are also indicated by A_2'' and E′ for optical branches.

B. Three-component fermions and two-component Weyl fermions in the electronic structures

We have elucidated the electronic band structures of these nine compounds. Interestingly, they are in similarity to the case of ZrTe in Ref. [64]. As an example, the electronic band structure of ZrSe is given in the Supplemental Fig. S1 [119], indicating the coexisted fermions, TDNPs and WPs, whose coordinators are further compiled in Fig. 1(c). Of course, the similar electronic behaviors can be observed for other compounds, but TiS is unique. Because of its rather weak spin-orbit coupling (SOC) effect, TiS exhibits the coexistence of six DNLs and two sixfold degenerate nodal points of its electronic structure in the BZ. This situation is exactly what happens for other eight compounds when the SOC effect is ignored. Basically, the appearance of these two types of fermions, TDNPs and WPs, in this family share the same physics, as previously discussed for ZrTe [64]. The details of their electronic structures and their topologically protected nontrivial surface states refer to Supplemental Figs. S1, S2, S3, and S4 [119] as well as the corresponding supplemental texts [119].

C. Triply degenerate nodal points (TDNPs) of the phonons in TiS, ZrSe, and HfTe

We have found that the presence of the triply degenerate nodal points (TDNPs) of the phonons in three compounds of TiS, ZrSe, and HfTe after a systemical analysis of their phonon dispersions (see Supplemental Fig. S5 [119]). Because each primitive cell contains two atoms [Fig. 1(a)], their phonon dispersions have six branches consisting of three acoustic and three optical ones, respectively. As compared with the computed phonon dispersions in Figs. 2(a)–2(c) and their phonon densities of states in Figs. 2(d)–2(f) of the isoelectronic ZrS, ZrSe, and ZrTe compounds, a well-separated acoustic-optical gap can be observed in both ZrS and ZrTe with the smallest direct gap at the A point $(0, 0, \pi/2)$ on the boundary of the BZ. The specified analysis uncovered that for both ZrS and ZrTe compounds the top phonon band of the gap at the A point is comprised with the doubly degenerate vibrational mode (corresponding to the *irrep* symbol E) of phonons in which both Zr and S (or Te) atoms, oppositely and collinearly, displace along either x or y direction [Mode$_=^{x,y}$ as marked in Fig. 1(b)]. The vibrational amplitude of the E Mode$_=^{x,y}$ is contributed nearly 100% by the Zr atom, rather than by S (or Te) atoms. The bottom phononic band of the gap at the A point is a singly degenerate mode A_1 at which both Zr and S (or Te) atoms collinearly move in the same k_z direction [Mode$_\perp^z$ as marked in Fig. 1(a)]. But its amplitude of this Mode$_\perp^z$ is almost fully dominated by the displacement of S (or Te) atoms.

In contrast to both ZrS and ZrTe in Fig. 2, the case of ZrSe shows no acoustic-optical gap [Fig. 2(b)], as illustrated by its phonon density of states in Fig. 2(e). It has been noted that the planar E Mode$_=^{x,y}$ at the A point becomes now lower in frequency than the A_1 Mode$_\perp^z$. Accordingly, this fact corresponds to the occurrence of phonon band inversion at the A point. It means the unusual fact that around the A point the optical phonon bands invert below the acoustic band which normally should have a lower frequency. Physically, within the (quasi)harmonic approximation the vibrational frequency ω has to be proportional to $\sqrt{\beta/m}$ at the boundary of the BZ. Here, β is the second-order force constant—the second derivative of the energy following a given vibrational mode as a function of the displacement and m the atomic mass. At the zone boundary A point, both $\beta_=$ and $m_=$ refer to the second force constant and atomic mass associated with the E Mode$_=^{x,y}$, whereas both $\beta_\perp$ and $m_\perp$ correspond to those of the A_1Mode$_\perp^z$. Therefore, as seen in Fig. 2(b) for ZrSe the occurrence of the phonon band inversion at the boundary A point is certainly induced by both β and m which are determined by the planar E Mode$_=^{x,y}$ and the A_1Mode$_\perp^z$ at the A point. Following this consideration, we have defined the dimensionless ratio τ as follows,

$$\tau = \frac{\sqrt{\beta_=/m_=}}{\sqrt{\beta_\perp/m_\perp}}, \tag{1}$$

where τ specifies the comparison between the frequencies of both Mode$_=^{x,y}$ and Mode$_\perp^z$. With $\tau > 1$ the material shows no band inversion, thereby indicating no TDNPs. $\tau < 1$ implies the appearance of the phonon band inversion with the TDNPs

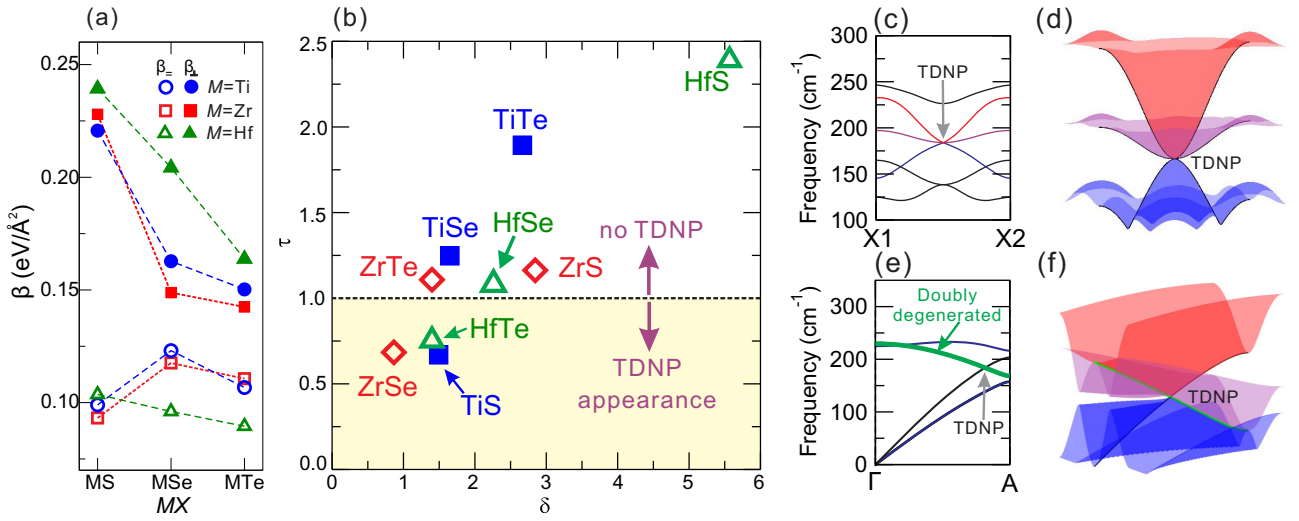

FIG. 3. Second-order force constant at the A point and the dimensionless ratio τ of *MX*. Panel (a): DFT-derived second-order force constant at the A point for both the two-fold degenerate planar vibrational Mode$_{=}^{x,y}$ and the vibrational Mode$_{\perp}^{z}$. Panel (b): The derived parameter τ from Eq. (1) as a function of the δ value, as defined in the main text, for all nine compounds. Panels (c) and (e): DFT-derived phonon dispersions to elucidate phonon TDNPs of ZrSe along the X1 $(-\pi/2, 0, 0)$ to X2 $(\pi/2, 0, 0)$ and Γ-A directions, respectively. Panels (d) and (f): Zoom-in 3D visualization of phonon TDNPs in the $k_z = 0$ and $k_y = 0$ planes, respectively.

in the acoustic and optical gap. With such a definition, we further plot the β with the sequence of ZrS, ZrSe, and ZrTe in Fig. 3(a). It has been found that, only with the second-order force constants of $\beta_{=}$ and $\beta_{\perp}$ [Fig. 3(a)] it is not enough to induce the phonon band inversion. This fact is in agreement with the Eq. (1) although the difference between $\beta_{=}$ and $\beta_{\perp}$ is the smallest in ZrSe among them in Fig. 3(a). Furthermore, for all nine compounds in this family we compiled their τ values as a function of the ratio (δ) of the atomic masses related with Mode$_{=}^{x,y}$ over Mode$_{\perp}^{z}$ [namely, $\delta = m(\text{Mode}_{=}^{x,y})/m(\text{Mode}_{\perp}^{z})$] in Fig. 3(b). This implies that, if the atomic masses of constituents in a targeted material highly differ, the possibility to have TDNPs in the acoustic and optical gap of its phonon dispersion is extremely low. However, if they have the comparable atomic masses with the δ ratio close to 1 the possibility to have TDNPs is high in the acoustic and optical gap. Following this model, we have further uncovered that, because the τ value is smaller than 1, both TiS and HfTe have similar property as what ZrSe does [Fig. 3(b)]. The findings for both TiS and HfTe are in accordance with the DFT-derived phonon dispersions in Supplemental Fig. S5 [119]. However, there is no TDNP in the acoustic and optical gap of the other members. These facts imply that in these materials the difference between the atomic masses of constituents in the compound plays a key role in inducing the phonon band inversion for the appearance of TDNPs in the acoustic and optical gap, as seen for three cases of TiS, ZrSe, and HfTe whose δ value are all around 1.

Importantly, as accompanying with the occurrence of the phonon band inversion, the TDNPs, featured by a linear crossing of the frequencies between the acoustic and optical bands, unavoidably appear at $(0, 0, k_z = \pm 0.40769)$ along the Γ-A direction in the BZ [Fig. 2(b) and Fig. 3] for ZrSe. Their appearance of the TDNPs in the acoustic and optical gap is indeed protected by the C_{3z} rotation and mirror symmetries along the Γ-A direction because C_{3z} allows the coexistence of twofold (Mode$_{=}^{x,y}$) and onefold (Mode$_{\perp}^{Z}$) representations, in similarity to their electronic band structures as discussed above. To elucidate the underlying mechanism of the phonon TDNPs in the acoustic and optical gap, it still needs to be emphasized that, on one hand, the rotation and mirror symmetries substantially provide the prerequisite to produce these two competing modes (twofold Mode$_{=}^{x,y}$ and onefold Mode$_{\perp}^{Z}$) and, on the other hand, the comparable atomic masses of constituent elements are another ingredient to trigger the phononic band inversion. Of course, at this TDNP it still implies that the planar Mode$_{=}^{x,y}$ and the Mode$_{\perp}^{Z}$ at $(0, 0, k_z = \pm 0.40769)$ locate at the strictly same frequency of 183.9 cm^{-1}. The TDNPs locate at $(0, 0, k_z = \pm 0.40382)$ with the frequency of 293.4cm^{-1} for TiS and at $(0, 0, k_z = \pm 0.43045)$ with the frequency of 133.3cm^{-1} for HfTe. To elucidate the 3D TDNP shape of ZrSe, we also plot the zoom-in dispersions on both $k_z = 0$ and $k_y = 0$ planes of BZ in Fig. 3. From both Figs. 3(c) and 3(d) in the $k_z = 0$ the TDNP in the acoustic and optical gap can be clearly visualized to have an isotropic shape. However, in the $k_y = 0$ plane the phonon bands around the TDNPs are highly complex with the helicoid shape [Figs. 3(e) and 3(f)]. Recently, the similar TDNPs also exist between doubly degenerate E_{1u} mode and singly degenerate acoustic mode along the Γ-A direction for high-temperature superconductor MgB_2 [89].

D. Two-component Weyl phonons in TiS, ZrSe, and HfTe

Besides the existence of the TDNPs in TiS, ZrSe, and HfTe, the calculations revealed the occurrence of the two-component Weyl nodes (WPs) in their phonon spectra. As evidenced in Fig. 4(a) for TiS, the phonon bands have five different band crossings (from C1 to C5) at the high-symmetry K point and a band crossing at the H point. In particular, because these crossings are not constrained by any mirror symmetry, they result in the appearance of six pairs of WPs (Table I). Among them, the band crossings from C1 to C5 confirm the five pairs of type-I WPs from WP1 to WP5 and the C6 crossing gives rise

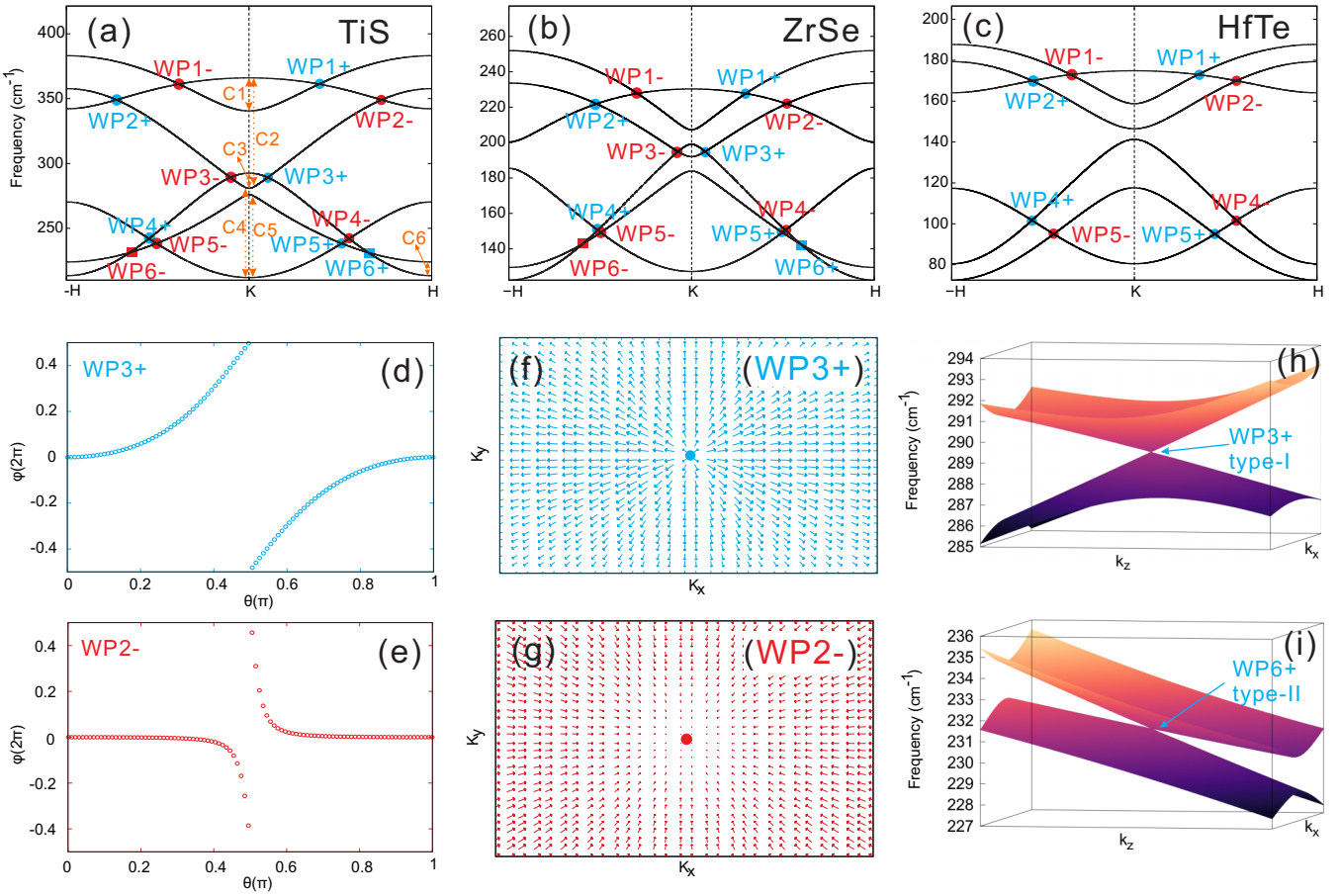

FIG. 4. Topological phonons of TiS, ZrSe, and HfTe. Panels (a), (b), and (c): DFT-derived phonon dispersions along K to H for TiS, ZrSe, and HfTe, respectively. Panels (d) and (e) show the Wannier center evolutions around positive charge WP3+ and negative charge WP2− nodes for TiS, respectively. Panels (g) and (f) denote the Berry curvature distributions around WP3+ and WP2− Weyl nodes for TiS. Panels (h) and (i) show the phonon dispersions around a type-I WP3+ and a type-II WP6+ Weyl node for TiS, respectively. Noted that the symbols of WP1 ∼ WP6 are the Weyl nodes, the symbols of C1 to C6 refer to six different band crossings, and the signs of + and − denote the topological positive and negative charges, respectively.

to the sixth pair of type-II WP6 one. The phonon dispersions of type-I and type-II WPs are shown in Fig. 4(h) and Fig. 4(i), respectively. To identify their topological nontrivial properties, we have calculated the topological charge of each Weyl node, which is defined by the integration of Berry curvature using a closed surface surrounding a node within the framework of the Wilson-loop method [109,110]. For instance, Figs. 4(d) and 4(e) show the Wannier center evolutions around WP3+ and WP2− with the topological positive and negative charges, respectively. Their corresponding Berry curvatures are shown in Figs. 4(f) and 4(g), indicating that the positive and negative charges, WP3+ and WP2−, have different winding directions of their Berry curvatures. Furthermore, we determine the charges of all the WPs of TiS in Table I. In similarity, ZrSe shares the same six pairs of WPs (5 pairs of type-I ones and a pair of type-II one) in Fig. 4(b) whereas HfTe only has four pairs of type-I WPs in Fig. 4(c), whose coordinators are given in Table I. This difference is mainly because in HfTe the phonon dispersions from K to H are lacking two band crossings, C3 at K and C6 at H.

TABLE I. Weyl points at $\mathbf{k} = (\frac{1}{3}, \frac{1}{3}, k_z)$ and their frequencies ω, topological charges (+ or −) and types (type-I or type-II) of TiS, ZrSe, and HfTe.

WPs	k_z	ω (cm^{-1})	Charge	Type	k_z	ω (cm^{-1})	Charge	Type	k_z	ω (cm^{-1})	Charge	Type
WP1	0.1919	361.22	+	I	0.1485	227.76	+	I	0.1739	172.95	+	I
WP2	0.3628	349.07	−	I	0.2600	221.91	−	I	0.2798	169.95	−	I
WP3	0.0517	289.21	+	I	0.0371	194.93	+	I				
WP4	0.2741	242.05	−	I	0.2569	150.52	−	I	0.2803	101.67	−	I
WP5	0.2533	238.37	+	I	0.2486	149.22	+	I	0.2205	94.99	+	I
WP6	0.3265	231.30	+	II	0.2977	142.84	+	II				

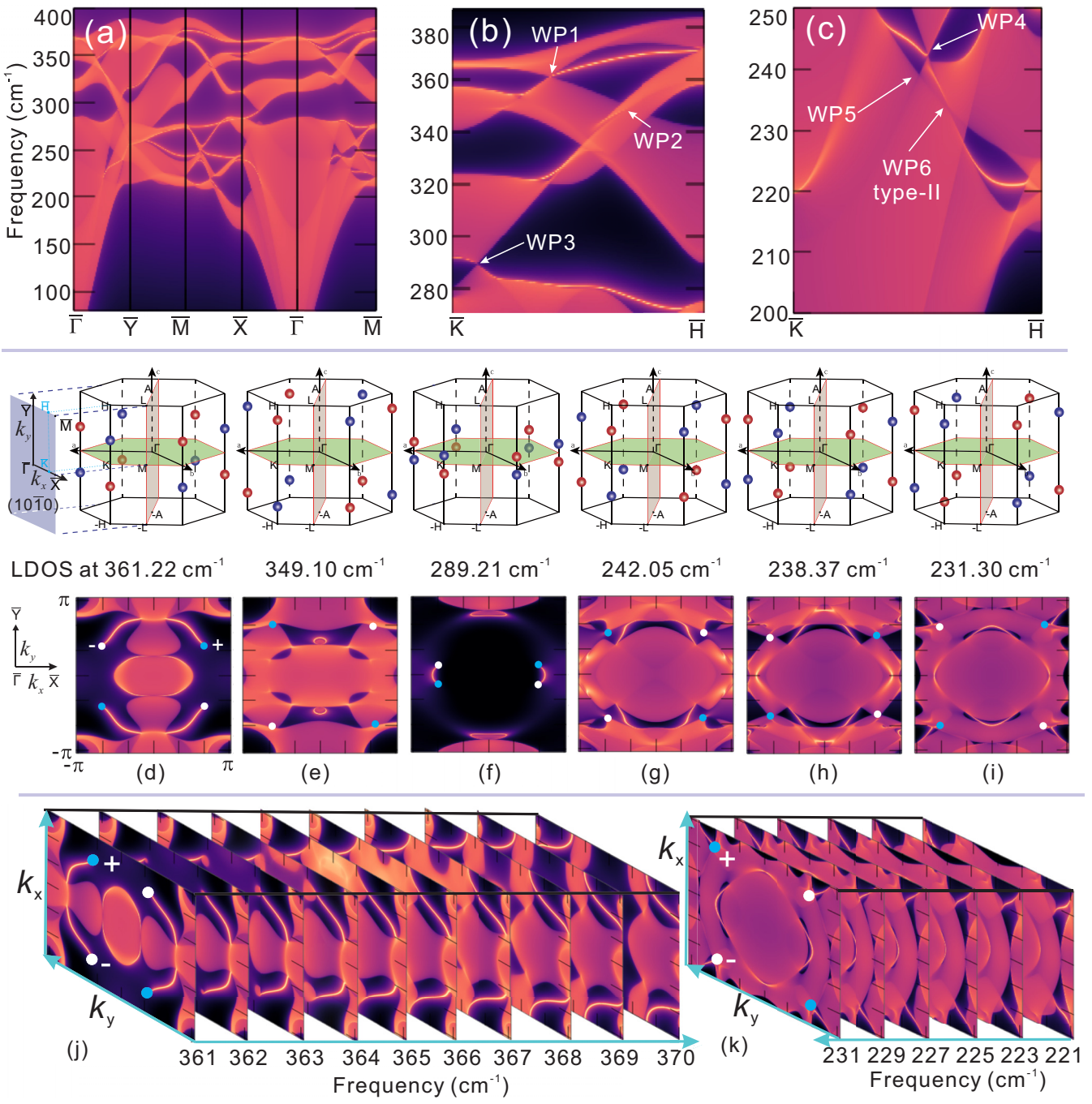

FIG. 5. The surface phonon spectra and the surface phonon densities of states (PDOSs) of the $(10\bar{1}0)$ surface of TiS. Panels (a), (b), and (c): the surface phonon spectra along the high-symmetry lines in panel (a) and along the defined $\bar{K}$-$\bar{H}$ line of the BZ in the $(10\bar{1}0)$ surface. Panels (d) and (e): the surface PDOSs at the six frequencies that the six pairs of Weyl nodes have and the projections of these bulk WPs are marked as solid blue (positive topological charge) and white (negative topological charge) circles in each panel. The surface opening arc states connect two WPs with opposite charges which can be visualized in panels (d)–(i). Panels (j) and (k): the frequency-dependent evolutions of the arc states connecting the type-I WP1 and the type-II WP6 on the $(10\bar{1}0)$ surface of TiS, respectively.

Certainly, the existence of these WPs gives rise to the topologically protected nontrivial surface states (TPSSs) of the surface phonon dispersions. As shown in Figs. 5(a)–5(c), we have calculated the surface phonon spectrum of the $(10\bar{1}0)$ surface of TiS along the high-symmetry momentum paths in the surface BZ. In particular, in order to see the projections of all WPs on the $(10\bar{1}0)$ surface, we have plotted the surface phonon dispersions [Figs. 5(b) and 5(c)] along the $\bar{K}$-$\bar{H}$ direction, as defined in the $(10\bar{1}0)$ surface BZ [Fig. 5(d)]. This $\bar{K}$-$\bar{H}$ direction indeed is the projection of the K-H direction in the bulk BZ. As evidenced in Fig. 5(b), the three type-I WPs, WP1, WP2, and WP3, are clearly demonstrated and the other two type-I WP4 and WP5 as well as another type-II WP6 can be apparently seen in Fig. 5(c). Accordingly, we have observed

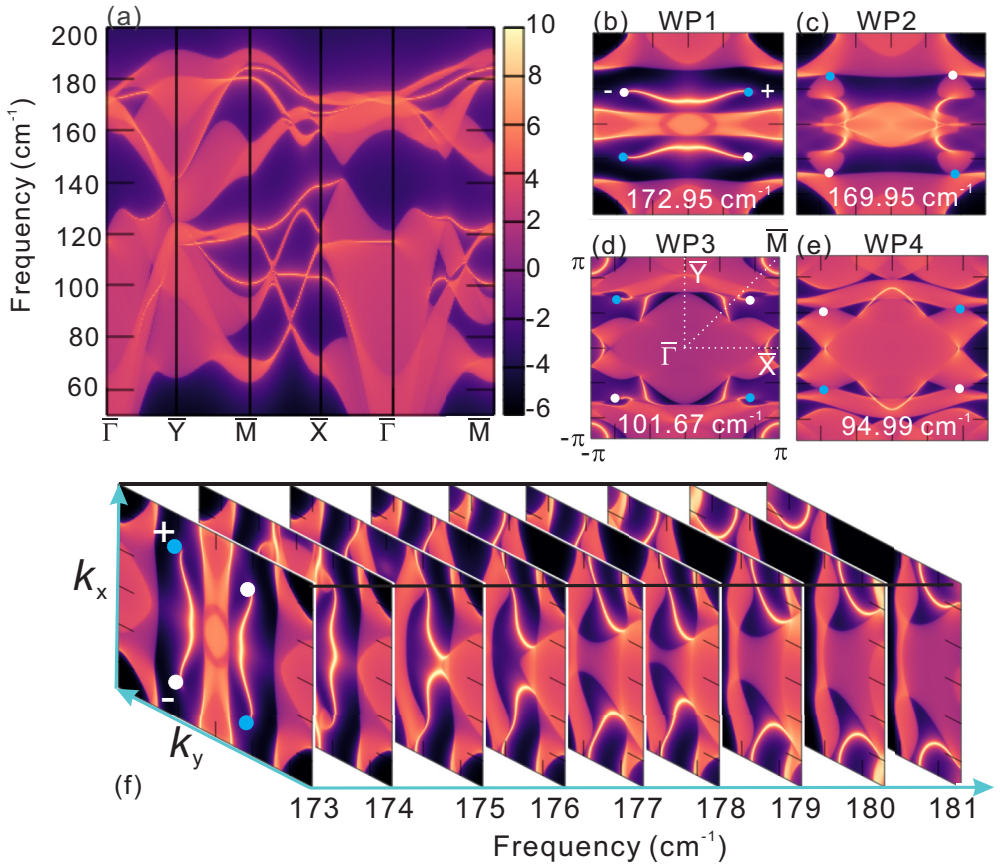

FIG. 6. The surface phonon dispersion and its evolution of the PDOSs on the $(10\bar{1}0)$ surface of HfTe. Panel (a): The surface phonon dispersion on the $(10\bar{1}0)$ surface of HfTe. Panels (b)–(e): The surface phonon densities of states (PDOS) at the frequencies of four pairs of Weyl nodes (WP1, WP2, WP4, and WP5 in HfTe). The projections (solid white circles—negative charge and solid blue circles—positive charge) of the bulk WPs (and their symmetric counterparts) on the $(10\bar{1}0)$ surface are indicated on each figure. The surface arcs connect two WPs with opposite charges. Panel (f): the frequency-dependent evolutions of the arc states connecting the type-I WP1 on the $(10\bar{1}0)$ surface of HfTe.

the interesting TPSSs, which are typically connecting each WP in Figs. 5(b) and 5(c). We further plot their 2D visualization of their phonon density of states (PDOSs) in Figs. 5(d)–5(i) using the exact frequencies with 361.22 cm^{-1} of WP1, 349.10 cm^{-1} of WP2, 289.21 cm^{-1} of WP3, 242.05 cm^{-1} of WP4, 238.37 cm^{-1} of WP5, and 231.30 cm^{-1} of WP6, respectively. Interestingly, at each frequency for the $(10\bar{1}0)$ surface in Figs. 5(d)–5(i), the TPSSs featured by the broken surface arcs connecting two WPs with opposite charges for WP1, WP2, WP3, and WP6 can be clearly visualized. However, it is a bit difficult to observe the broken arcs states connecting WP4 and WP5 on the $(10\bar{1}0)$ surface because they are heavily overlapped with the projections of bulk phonon states. The case of ZrSe also exhibits the quite similar arc states of surface phonon on its $(10\bar{1}0)$ surface (not shown here).

As compared with both cases of TiS and ZrSe, HfTe exhibits some differences. HfTe only has four pairs of type-I WPs as marked in Fig. 4(c) and no type-II WPs. Figure 6 shows its phonon spectrum of the $(10\bar{1}0)$ surface and the 2D visualizations of the PDOSs with the frequencies of 172.95 cm^{-1} of WP1, 169.95 cm^{-1} of WP2, 101.67 cm^{-1} of WP4, and 94.99 cm^{-1} of WP5, respectively. The bulk WPs are also projected onto the $(10\bar{1}0)$ surface. As shown in Fig. 6(b), the broken arc states of the TPSSs are clearly linked to the pair of WP1 with opposite topological charges, and only partial for both WP2 and WP4 in Figs. 6(c) and 6(d), and not observable for WP5 due to its overlapping with the projected states of bulk phonon dispersions in Fig. 6(e). In addition, it still needs to be emphasized that the arc states can be certainly observed on some other planes which are paralleling to the bulk H-K direction, such as the $(01\bar{1}0)$ plane. However, note that the arc states connecting Weyl nodes cannot be observable on the (0001) surface because, on it, the projections of the K-H direction coincide at the same surface momentum, and their topological charges cancel each other.

IV. DISCUSSIONS

Through the DFT-derived results, these three materials of TiS, ZrSe, and HfTe are highly attractive because of the occurrence of the coexisted TDNPs and WPs. In the first, the TDNPs of their phonons are interesting because (i) they provide a good platform to study the behaviors of the basic triple degenerate boson, one of elementary particles, in the real materials, (ii) they are highly robust, which are locked by the threefold rotational symmetry of the hexagonal lattices, and (iii) they exactly occur in the optical-acoustic gap and do not overlap with other phonon bands. Perhaps, the thermal-excited signals related with these TDNPs will not be interfered by

other vibrational modes, thereby highlighting the viable cases to experimentally probe the TDNP-related properties.

In the second, it is well known that in the electronic structures the WPs and their associated topological invariants enable the corresponding materials to exhibit a variety of novel properties, such as robust surface states and chiral anomaly [22–34,36–41]. In our current cases, the existence of the bulk phononic WPs and their robust TPSSs render them to be very charming for possible applications, because these states cannot be backscattered. In particular, as evidenced in Fig. 5(j) the surface broken arc states connecting a pair of WP1 nodes in TiS exhibit a nearly one-way propagation. Its evolution further extends and shifts to the zone boundary with increasing the frequencies in a relatively wide region of frequency in Fig. 5(j). In similarity, the nearly one-way arc states connecting a pair of WP1 nodes in HfTe can be clearly visualized in Fig. 6(f). However, the evolution of the surface arc states connecting a pair of type-II WP6 in TiS cannot be fully visualized because most of them are overlapped with the projections of the bulk phonon states in Fig. 5(k). It needs to be emphasized that this topologically protected one-way propagation in these compounds are certainly robust and immune to defects. Within this context, utilizing the frequency around the WPs it is possible to provide directional selectivity for conducting heat (phonon) within the THz scales from the atomistic crystals. For instance, it would hence be promising to utilize them to propagate phononic vibrational waves along some specified directions or surfaces for applications of direction (or surface)-orientation thermal conduction and anisotropic thermoelectricity for innovative devices, or of acoustic devices in soundproofing and sonar stealth systems.

V. SUMMARY

Summarizing, through first-principles calculations we have revealed that three WC-type materials of TiS, ZrSe, and HfTe host both three-component bosons featured by TDNPs and two-component Weyl bosons featured by WPs in their phonon spectra. In both TiS and ZrSe, there exist six pairs of bulk WPs (five type-I nodes and one type-II node) locating at the K-H line in the BZ, whereas in HfTe only four pairs of type-I WPs exist. We have demonstrated that the phonon spectra of these three cases are topological in nature, exhibiting that the topologically protected nontrivial surface arc states of phonons. These nontrivial states are directly linked with various WPs with opposite chirality. Interestingly, these three cases still exhibit three-component fermions featured by TDNPs and six pairs of two-component Weyl fermions (WPs) in their electronic structures of the bulk crystals. The coexistence of the main features are (i) three-component phonons, (ii) two-component Weyl phonons and three-component fermions, and (iii) two-component Weyl fermions and, in particular, both three-component bosons and three-component fermions at the nearly same momentum [Figs. 1(c) and 1(d)] along the Γ-A direction could couple to each other through electron-phonon interactions. They hence highlight a wonderful platform to study the interplays between different types of topological electron excitations and topological phonons within the atomistic scale for potential multifunctionality quantum-mechanical properties.

ACKNOWLEDGMENTS

We thank H. M. Weng for valuable discussions. Work was supported by the National Science Fund for Distinguished Young Scholars (No. 51725103), by the National Natural Science Foundation of China (Grants No. 51671193 and No. 51474202), and by the Science Challenging Project No. TZ2016004. All calculations have been performed on the high-performance computational cluster in the Shenyang National University Science and Technology Park and the National Supercomputing Center in Guangzhou (TH-2 system) with a special program for applied research of the NSFC-Guangdong Joint Fund (the second phase) under Grant No. U1501501.

J.L., Q.X., and S.U. contributed equally to this work.

[1] C. L. Kane and E. J. Mele, Z_2 Topological Order and the Quantum Spin Hall Effect, Phys. Rev. Lett. **95**, 146802 (2005).

[2] M. Z. Hasan and C. L. Kane, Colloquium: Topological insulators, Rev. Mod. Phys. **82**, 3045 (2010).

[3] X.-L. Qi and S.-C. Zhang, Topological insulators and superconductors, Rev. Mod. Phys. **83**, 1057 (2011).

[4] H. M. Weng, X. Dai, and Z. Fang, Topological semimetals predicted from first-principles calculations, J. Phys.: Condens. Matter **28**, 303001 (2016).

[5] B. H. Yan and C. Felser, Topological Materials: Weyl semimetals, Annu. Rev. Condens. Matter Phys. **8**, 337 (2016).

[6] C.-K. Chiu, J. C. Y. Teo, A. P. Schnyder, and S. Ryu, Classification of topological quantum matter with symmetries, Rev. Mod. Phys. **88**, 035005 (2016).

[7] A. Bansil, H. Lin, and T. Das, Colloquium: Topological band theory, Rev. Mod. Phys. **88**, 021004 (2016).

[8] S. Rao, Weyl semi-metals : A short review, arXiv:1603.02821.

[9] Z. J. Wang, Y. Sun, X.-Q. Chen, C. Franchini, G. Xu, H. M. Weng, X. Dai, and Z. Fang, Dirac semimetal and topological phase transitions in A_3Bi(A = Na, K, Rb), Phys. Rev. B **85**, 195320 (2012).

[10] S. M. Young, S. Zaheer, J. C. Y. Teo, C. L. Kane, E. J. Mele, and A. M. Rappe, Dirac Semimetal in Three Dimension, Phys. Rev. Lett. **108**, 140405 (2012).

[11] Z. Wang, H. M. Weng, Q. Wu, X. Dai, and Z. Fang, Three dimensional Dirac semimetal and quantum transport in Cd_3As_2, Phys. Rev. B **88**, 125427 (2013).

[12] X. Y. Cheng, R. H. Li, Y. Sun, X.-Q. Chen, D. Z. Li, and Y. Y. Li, Ground-state phase in the three-dimensional topological Dirac semimetal Na_3Bi, Phys. Rev. B **89**, 245201 (2014).

[13] X. Y. Cheng, R. H. Li, D. Z. Li, Y. Y. Li, and X.-Q. Chen, Combined fast reversible liquidlike elastic deformation with topological phase transition in Na_3Bi, Phys. Rev. B **92**, 155109 (2015).

[14] M. Neupane, S.-Y. Xu, R. Sankar, N. Alidoust, G. Bian, C. Liu, I. Belopolski, T.-R. Chang, H.-T. Jeng, H. Lin, A. Bansil, F. Chou, and M. Z. Hasan, Observation of a three-dimensional topological Dirac semimetal phase in high-mobility Cd_3As_2, Nat. Commun. **5**, 3786 (2014).

[15] Z. K. Liu, J. Jiang, B. Zhou, Z. J. Wang, Y. Zhang, H. M. Weng, D. Prabhakaran, S.-K. Mo, H. Peng, P. Dudin, T. Kim, M. Hoesch, Z. Fang, X. Dai, Z. X. Shen, D. L. Feng, Z. Hussain, and Y. L. Chen, A stable three-dimensional topological Dirac semimetal Cd_3As_2, Nat. Mater. **13**, 677 (2014).

[16] Z. K. Liu, B. Zhou, Y. Zhang, Z. J. Wang, H. M. Weng, D. Prabhakaran, S.-K. Mo, Z. X. Shen, Z. Fang, X. Dai, Z. Hussain, and Y. L. Chen, Discovery of a Three-Dimensional Topological Dirac Semimetal, Na_3Bi, Science **343**, 864 (2014).

[17] B. J. Yang and N. Nagaosa, Classification of stable three dimensional Dirac semimetals with nontrivial topology, Nat. Commun. **5**, 4898 (2014).

[18] X. Y. Cheng, R. H. Li, D. Z. Li, Y. Y. Li, and X.-Q. Chen, Stable compositions and structures in the Na-Bi system, Phys. Chem. Chem. Phys. **17**, 6933 (2015)

[19] S.-Y. Xu, C. Liu, S. K. Kushwaha, R. Sankar, J. W. Krizan, I. Belopolski, M. Neupane, G. Bian, N. Alidoust, T. R. Chang, H. T. Jeng, C. Y. Huang, W. F. Tsai, H. Lin, P. P. Shibayev, F. C. Chou, R. J. Cava, and M. Z. Hasan, Observation of Fermi arc surface states in a topological metal, Science **347**, 294 (2015).

[20] Y. Du, B. Wan, D. Wang, L. Sheng, C. G. Duan, and X. G. Wan, Dirac and Weyl Semimetal in XYBi (X= Ba, Eu; Y= Cu, Ag and Au), Sci. Rep. **5**, 14423 (2015).

[21] J. Hu, Y. L. Zhu, D. Graf, Z. J. Tang, J. Y. Liu, and Z. Q. Mao, Quantum oscillation studies of topological semimetal candidate ZrGeM (M=S, Se, Te), Phys. Rev. B **95**, 205134 (2017).

[22] S. Murakami, Phase transition between the quantum spin Hall and insulator phases in 3D: Emergence of a topological gapless phase, New J. Phys. **9**, 356 (2007).

[23] X. G. Wan, A. M. Turner, A. Vishwanath, and S. Y. Savrasov, Topological semimetal and Fermi-arc surface states in the electronic structure of pyrochlore iridates, Phys. Rev. B **83**, 205101 (2011).

[24] G. Xu, H. M. Weng, Z. Wang, X. Dai, and Z. Fang, Chern Semimetal and the Quantized Anomalous Hall Effect in $HgCr_2Se_4$, Phys. Rev. Lett. **107**, 186806 (2011).

[25] S.-Y. Xu, N. Alidoust, I. Belopolski, Z. Yuan, G. Bian, T.-R. Chang, H. Zheng, V. N. Strocov, D. S. Sanchez, G. Chang, C. Zhang, D. Mou, Y. Wu, L. Huang, C.-C. Lee, S.-M. Huang, B. Wang, A. Bansil, H.-T. Jeng, T. Neupert, A. Kaminski, H. Lin, S. Jia, and M. Z. Hasan, Discovery of a Weyl fermion state with Fermi arcs in niobium arsenide, Nat. Phys. **11**, 748 (2015).

[26] C. Shekhar, A. K. Nayak, Y. Sun, M. Schmidt, M. Nicklas, I. Leermakers, U. Zeitler, Y. Skourski, J. Wosnitza, Z. K. Liu, Y. L. Chen, W. Schnelle, H. Borrmann, Y. Grin, C. Felser, and B. H. Yan, Extremely large magnetoresistanceand ultrahigh mobility in the topological Weyl semimetal candidate NbP, Nat. Phys. **11**, 645 (2015).

[27] S.-Y. Xu, I. Belopolski, D. S. Sanchez, C. Guo, G. Chang, C. Zhang, G. Bian, Z. Yuan, H. Lu, Y. Feng, T.-R. Chang, P. P. Shibayev, M. L. Prokopovych, N. Alidoust, H. Zheng, C.-C. Lee, S.-M. Huang, R. Sankar, F. Chou, C.-H. Hsu, H.-T. Jeng, A. Bansil, T. Neupert, V. N. Strocov, H. Lin, S. Jia, and M. Z. Hasan, Experimental discovery of a topological Weyl semimetal state in TaP, Sci. Adv. **1**, e1501092 (2015).

[28] H. M. Weng, C. Fang, Z. Fang, B. A. Bernevig, and X. Dai, Weyl Semimetal Phase in Noncentrosymmetric Transition-Metal Monophosphides, Phys. Rev. X **5**, 011029 (2015).

[29] S. M. Huang, S. Y. Xu, I. Belopolski, C. C. Lee, G. Chang, B. K. Wang, N. Alidoust, G. Bian, M. Neupane, C. Zhang, S. Jia, A. Bansil, H. Lin, and M. Z. Hasan, A Weyl Fermion semimetal with surface Fermi arcs in the transition metal monopnictide TaAs class, Nat. Commun. **6**, 7373 (2015).

[30] B. Q. Lv, H. M. Weng, B. B. Fu, X. P. Wang, H. Miao, J. Ma, P. Richard, X. C. Huang, L. X. Zhao, G. F. Chen, Z. Fang, X. Dai, T. Qian, and H. Ding, Experimental Discovery of Weyl Semimetal TaAs, Phys. Rev. X **5**, 031013 (2015).

[31] B. Q. Lv, N. Xu, H. M. Weng, J. Z. Ma, P. Richard, X. C. Huang, L. X. Zhao, G. F. Chen, C. E. Matt, F. Bisti, V. N. Strocov, J. Mesot, Z. Fang, X. Dai, T. Qian, M. Shi, and H. Ding, Observation of Weyl nodes in TaAs, Nat. Phys. **11**, 724 (2015).

[32] S.-Y. Xu, I. Belopolski, N. Alidoust, M. Neupane, G. Bian, C. Zhang, R. Sankar, G. Chang, Z. Yuan, C.-C. Lee, S.-M. Huang, H. Zheng, J. Ma, D. S. Sanchez, B. Wang, A. Bansil, F. C. Chou, P. P. Shibayev, H. Lin, S. Jia, and M. Z. Hasan, Discovery of a Weyl fermion semimetal and topological Fermi arcs, Science **349**, 613 (2015).

[33] L. Yang, Z. Liu, Y. Sun, H. Peng, H. Yang, T. Zhang, B. Zhou, Y. Zhang, Y. Guo, M. Rahn, D. Prabhakaran, Z. Hussain, S.-K. Mo, C. Felser, B. H. Yan, and Y. L. Chen, Weyl semimetal phase in the non-centrosymmetric compound TaAs, Nat. Phys. **11**, 728 (2015).

[34] Y. Zhang, D. Bulmash, P. Hosur, A. C. Potter, and A. Vishwanath, Quantum oscillations from generic surface Fermi arcs and bulk chiral modes in Weyl semimetals, Sci. Rep. **6**, 23741 (2016).

[35] Y. Xu, F. Zhang, and C. W. Zhang, Structured Weyl Points in Spin-Orbit Coupled Fermionic Superfluids, Phys. Rev. Lett. **115**, 265304 (2015).

[36] A. A. Soluyanov, D. Gresch, Z. J. Wang, Q. Wu, M. Troyer, X. Dai, and B. A. Bernevig, Type-II Weyl semimetals, Nature (London) **527**, 495 (2015).

[37] S.-Y. Xu, N. Alidoust, G. Q. Chang, H. Lu, B. Singh, I. Belopolski, D. S. Sanchez, X. Zhang, G. Bian, H. Zheng, M.-A. Husanu *et al.*, Discovery of Lorentz-violating type II Weyl fermions in LaAlGe, Sci. Adv. **3**, e1603266 (2017).

[38] G. Chang, B. Singh, S. Y. Xu, G. Bian, S. M. Huang, C. H. Hsu, I. Belopolski, N. Alidoust, D. S. Sanchez, H. Zheng, and H. Lu, Magnetic and noncentrosymmetric Weyl fermion semimetals in the RAlX family of compounds (R = rare earth, Al = aluminium, X = Si, Ge), Phys. Rev. B **97**, 041104(R) (2018).

[39] H. Yang, Y. Sun, Y. Zhang, W. J. Shi, S. S. Parkin, and B. H. Yan, Topological Weyl semimetals in the chiral antiferromagnetic materials Mn_3Ge and Mn_3Sn, New J. Phys. **19**, 015008 (2017).

[40] B. Singh, A. Sharma, H. Lin, M. Z. Hasan, R. Prasad, and A. Bansil, Topological electronic structure and Weyl semimetal in the $TlBiSe_2$ class of semiconductors, Phys. Rev. B **86**, 115208 (2012).

[41] J. Ruan, S. K. Jian, H. Yao, H. Zhang, S. C. Zhang, and D. Xing, Symmetry-protected ideal Weyl semimetal in HgTe-class materials, Nat. Commun. **7**, 11136 (2016).

[42] D. T. Son and B. Z. Spivak, Chiral anomaly and classical negative magnetoresistance of Weyl metals, Phys. Rev. B **88**, 104412 (2013).

[43] X. Huang, L. Zhao, Y. Long, P. Wang, D. Chen, Z. Yang, H. Liang, M. Xue, H. M. Weng, Z. Fang, X. Dai, and G.

Chen, Observation of the Chiral-Anomaly-Induced Negative Magnetoresistance in 3D Weyl Semimetal TaAs, Phys. Rev. X **5**, 031023 (2015).
[44] P. Hosur and X. Qi, Recent developments in transport phenomena in Weyl semimetals, C. R. Phys. **14**, 857 (2013).
[45] C. Fang, H. M. Weng, X. Dai, and Z. Fang, Topological nodal line semimetals, Chin. Phys. B **25**, 117106 (2016).
[46] R. H. Li, H. Ma, X. Y. Cheng, S. L. Wang, D. Z. Li, Z. Y. Zhang, Y. Y. Li, and X.-Q. Chen, Dirac Node Lines in Pure Alkali Earth Metals, Phys. Rev. Lett. **117**, 096401 (2016).
[47] J. X. Li, H. Ma, Q. Xie, S. B. Feng, S. Ullah, R. Li, J. Dong, D. Z. Li, Y. Y. Li, and X.-Q. Chen, Topological quantum catalyst: Dirac nodal line states and a potential catalyst of hydrogen evolution in the TiSi family, Sci. China Mater. **61**, 23 (2018).
[48] S. Ryu and Y. Hatsugai, Topological Origin of Zero-Energy Edge States in Particle-Hole Symmetric Systems, Phys. Rev. Lett. **89**, 077002 (2002).
[49] T. T. Heikkilä and G. E. Volovik, Dimensional crossover in topological matter: Evolution of the multiple Dirac point in the layered system to the flat band on the surface, JETP Lett. **93**, 59 (2011).
[50] A. A. Burkov, M. D. Hook, and L. Balents, Topological nodal semimetals, Phys. Rev. B **84**, 235126 (2011).
[51] H. M. Weng, Y. Y. Liang, Q. N. Xu, R. Yu, Z. Fang, X. Dai, and Y. Kawazoe, Topological node-line semimetal in three dimensional graphene networks, Phys. Rev. B **92**, 045108 (2015).
[52] R. Yu, H. M. Weng, Z. Fang, X. Dai, and X. Hu, Topological Node-Line Semimetal and Dirac Semimetal State in Antiperovskite. Cu_3PdN, Phys. Rev. Lett. **115**, 036807 (2015).
[53] Y. Kim, B. J. Wieder, C. L. Kane, and A. M. Rappe, Dirac Line Nodes in Inversion-Symmetric Crystals, Phys. Rev. Lett. **115**, 036806 (2015).
[54] L. S. Xie, L. M. Schoop, E. M. Seibel, Q. D. Gibson, W. W. Xie, and R. J. Cava, A new form of Ca_3P_2 with a ring of Dirac nodes, APL Materials **3**, 083602 (2015).
[55] M. G. Zeng, C. Fang, G. Q. Chang, Y.-A. Chen, T. Hsieh, A. Bansil, H. Lin, and L. Fu, Topological semimetals and topological insulators in rare earth monopnictides, arXiv:1504.03492.
[56] R. H. Li, Q. Xie, X. Y. Cheng, D. Z. Li, Y. Y. Li, and X.-Q. Chen, First-principles study of the large-gap three-dimensional topological insulators M_3Bi_2 (M = Ca, Sr, Ba), Phys. Rev. B **92**, 205130 (2015).
[57] K. Mullen, B. Uchoa, and D. T. Glatzhofer, Line of Dirac Nodes in Hyperhoneycomb Lattices, Phys. Rev. Lett. **115**, 026403 (2015).
[58] L.-Y. Gan, R. Wang, Y. J. Jin, D. B. Ling, J. Z. Zhao, W. P. Xu, J. F. Liu, and H. Xu, Pressure-induced topological Node-line semimetals in Alkaline-earth hexaborides XB_6 (X = Ca, Sr, Ba), arXiv:1611.06386.
[59] T. Kawakami and X. Hu, Symmetry-guaranteed nodal-line semimetals in an fcc lattice, Phys. Rev. B **96**, 235307 (2017).
[60] B. Yang, H. C. Zhou, X. M. Zhang, X. B. Liu, and M. W. Zhao, Dirac cones and highly anisotropic electronic structure of supergraphyne, Carbon **113**, 40 (2017).
[61] B. Bradlyn, J. Cano, Z. Wang, M. G. Vergniory, C. Felser, R. J. Cava, and B. A. Bernevig, Beyond Dirac and Weyl fermions: Unconventional quasiparticles in conventional crystals, Science **353**, 558 (2016).
[62] G. W. Winkler, Q. Wu, M. Troyer, P. Krogstrup, and A. A. Soluyanov, Topological Phases in $InAs_{1-x}Sb_x$: From Novel Topological Semimetal to Majorana Wire, Phys. Rev. Lett. **117**, 076403 (2016).
[63] H. M. Weng, C. Fang, Z. Fang, and X. Dai, Topological semimetals with triply degenerate nodal points in θ-phase tantalum nitride, Phys. Rev. B **93**, 241202 (2016).
[64] H. Weng, C. Fang, Z. Fang, and X. Dai, Coexistence of Weyl fermion and massless triply degenerate nodal points, Phys. Rev. B **94**, 165201 (2016).
[65] Z. Zhu, G. W. Winkler, Q. S. Wu, J. Li, and A. A. Soluyanov, Triple Point Topological Metals, Phys. Rev. X **6**, 031003 (2016).
[66] G. Chang, S. Y. Xu, S. M. Huang, D. S. Sanchez, C. H. Hsu, G. Bian, Z. M. Yu, I. Belopolski, N. Alidoust, H. Zheng, T. R. Chang, H. J. Jeng, S. A. Yang, T. Neupert, H. Lin, and M. Z. Hasan, New fermions on the line in topological symmorphic metals, Sci. Rep. **7**, 1688 (2017).
[67] J. B. He, D. Chen, W. L. Zhu, S. Zhang, L. X. Zhao, Z. A. Ren, and G. F. Chen, Magnetotransport properties of the triply degenerate node topological semimetal: tungsten carbide, Phys. Rev. B **95**, 195165 (2017).
[68] B. Q. Lv, Z. L. Feng, Q. N. Xu, X. Gao, J. Z. Ma, L. K. Kong, P. Richard, Y. B. Huang, V. N. Strocov, C. Fang, H. M. Weng, Y. G. Shi, T. Qian, and H. Ding, Observation of three-component fermions in the topological semimetal molybdenum phosphide, Nature (London) **546**, 627 (2017).
[69] H. Yang, J. B. Yu, S. S. P. Parkin, C. Felser, C.-X. Liu, and B. Yan, Prediction of Triple Point Fermions in Simple Half-Heusler Topological Insulators, Phys. Rev. Lett. **119**, 136401 (2017).
[70] J. B. Yu, B. H. Yan, and C.-X. Liu, Model Hamiltonian and time reversal breaking topological phases of anti-ferromagnetic half-Heusler Materials, Phys. Rev. B **95**, 235158 (2017).
[71] Z. J. Wang, A. Alexandradinata, R. J. Cava, and B. A. Bernevig, Hourglass fermions, Nature (London) **532**, 189 (2016).
[72] L. Lu, L. Fu, J. D. Joannopoulos, and M. Soljačić, Weyl points and line nodes in gyroid photonic crystals, Nature Photon. **7**, 294 (2013).
[73] L. Lu, Z. Wang, D. Ye, L. Ran, L. Fu, J. D. Joannopoulos, and M. Soljacic, Experimental observation of Weyl points, Science **349**, 622 (2015).
[74] S. D. Huber, Topological mechanics, Nat. Phys. **12**, 621 (2016).
[75] E. Prodan and C. Prodan, Topological Phonon Modes and their Role in Dynamic Instability of Microtubules, Phys. Rev. Lett. **103**, 248101 (2009).
[76] B. G. G. Chen, N. Upadhyaya, and V. Vitelli, Nonlinear conduction via solitons in a topological mechanical insulator, Proc. Natl. Acad. Sci. USA **111**, 13004 (2014).
[77] Z. Yang, F. Gao, X. Shi, X. Lin, Z. Gao, Y. Chong, and B. Zhang, Topological Acoustics, Phys. Rev. Lett. **114**, 114301 (2015).
[78] P. Wang, L. Lu, and K. Bertoldi, Topological Phononic Crystals with One-Way Elastic Edge Waves, Phys. Rev. Lett. **115**, 104302 (2015).
[79] M. Xiao, W. J. Chen, W. Y. He, and C. T. Chan, Synthetic gauge flux and Weyl points in acoustic systems, Nat. Phys. **11**, 920 (2015).
[80] L. M. Nash, D. Kleckner, A. Read, V. Vitelli, A. M. Turner, and W. T. Irvine, Topological mechanics of gyro-

scopic metamaterials, Proc. Natl. Acad. Sci. USA **112**, 14495 (2015).
[81] R. Susstrunk and S. D. Huber, Observation of phononic helical edge states in a mechanical topological insulator, Science **349**, 47 (2015).
[82] S. H. Mousavi, A. B. Khanikaev, and Z. Wang, Topologically protected elastic waves in phononic metamaterials, Nat. Commun. **6**, 8682 (2015).
[83] R. Fleury, A. B. Khanikaev, and A. AlRu, Floquet topological insulators for sound, Nat. Commun. **7**, 11744 (2016).
[84] D. Z. Rocklin, B. G. G. Chen, M. Falk, V. Vitelli, and T. Lubensky, Mechanical Weyl Modes in Topological Maxwell Lattices, Phys. Rev. Lett. **116**, 135503 (2016).
[85] C. He, X. Ni, H. Ge, X. C. Sun, Y. B. Chen, M.-H. Lu, X. P. Liu, and Y.-F. Chen, Acoustic topological insulator and robust one-way sound transport, Nat. Phys. **12**, 1124 (2016).
[86] R. Susstrunk and S. D. Huber, Classification of topological phonons in linear mechanical metamaterials, Proc. Natl. Acad. Sci. USA **113**, E4767 (2016).
[87] F. Li, X. Q. Huang, J. Y. Lu, J. H. Ma, and Z. Y. Liu, Weyl points and Fermi arcs in a chiral phononic crystal, Nat. Phys. **14**, 30 (2018).
[88] T. T. Zhang, Z. D. Song, A. Alexandradinata, H. M. Weng, C. Fang, L. Lu, and Z. Fang, Double-Weyl Phonons in Traisition-Metal Monosilicides, Phys. Rev. Lett. **120**, 016401 (2018).
[89] Q. Xie, J. X. Li, M. Liu, L. Wang, D. Z. Li, Y. Y. Li, and X.-Q. Chen, Phononic weyl nodal straight lines in high-temperature superconductor MgB_2, arXiv:1801.04048.
[90] Y. Liu, Y. Xu, S.-C. Zhang, and W. H. Duan, Model for topological phononics and phonon diode, Phys. Rev. B **96**, 064106 (2017).
[91] L. F. Zhang and Q. Niu, Chiral Phonons at High-Symmetry Points in Monolayer Hexagonal Lattices, Phys. Rev. Lett. **115**, 115502 (2015).
[92] P. Hohenberg and W. Kohn, Inhomogeneous Electron Gas, Phys. Rev. **136**, B864 (1964).
[93] W. Kohn, and L. J. Sham, Self-Consistent Equations Including Exchange and Correlation Effects, Phys. Rev. **140**, A1133 (1965).
[94] S. Baroni, S. D. Gironcoli, A. D. Corso, and P. Giannozzi, Phonons and related crystal properties from density-functional perturbation theory, Rev. Mod. Phys. **73**, 515 (2001).
[95] G. Kresse and J. Hafner, *Ab initio* molecular dynamics for liquid metals, Phys. Rev. B **47**, 558 (1993).
[96] G. Kresse, and J. Hafner, *Ab initio* molecular-dynamics simulation of the liquid-metal amorphous-semiconductor transition in germanium, Phys. Rev. B **49**, 14251 (1994).
[97] G. Kresse and J. Furthmüller, Efficiency of *ab-initio* total energy calculations for metals and semiconductors using a plane-wave basis set, Comput. Mater. Sci. **6**, 15 (1996).
[98] P. E. Blöhl Projector augmented-wave method, Phys. Rev. B **50**, 17953 (1994).
[99] G. Kresse and D. Joubert, From ultrasoft pseudopotentials to the projector augmented-wave method, Phys. Rev. B **59**, 1758 (1999).
[100] J. P. Perdew and Y. Wang, Accurate and simple analytic representation of the electron-gas correlation energy, Phys. Rev. B **45**, 13244 (1992).
[101] J. P. Perdew, K. Burke, and M. Ernzerhof, Generalized Gradient Approximation Made Simple, Phys. Rev. Lett. **77**, 3865 (1996).
[102] H. M. Weng, X. Dai, and Z. Fang, Exploration and prediction of topological electronic materials based on first-principles calculations, MRS Bull. **39**, 849 (2014).
[103] H. M. Weng, R. Yu, X. Hu, X. Dai, and Z. Fang, Quantum anomalous Hall effect and related topological electronic states, Adv. Phys. **64**, 227 (2015).
[104] M. P. Sancho, J. M. Sancho, and J. Rubio, Highly convergent schemes for the calculation of bulk and surface Green functions, J. Phys. F **15**, 851 (1985).
[105] N. Marzari and D. Vanderbilt, Maximally localized generalized Wannier functions for composite energy bands, Phys. Rev. B **56**, 12847 (1997).
[106] I. Souza, N. Marzari, and D. Vanderbilt, Maximally localized Wannier functions for entangled energy bands, Phys. Rev. B **65**, 035109 (2001).
[107] A. A. Mostofi, J. R. Yates, Y. S. Lee, I. Souza, D. Vanderbilt, and N. Marzari, Wannier90: A tool for obtaining maximally-localised Wannier functions, Comput. Phys. Commun. **178**, 685 (2008).
[108] L. Chaput, A. Togo, I. Tanaka, and G. Hug, Phonon-phonon interactions in transition metals, Phys. Rev. B **84**, 094302 (2011).
[109] R. Yu, X. L. Qi, A. Bernevig, Z. Fang, and X. Dai, Equivalent expression of Z_2 topological invariant for band insulators using the non-Abelian Berry connection, Phys. Rev. B **84**, 075119 (2011).
[110] A. A. Soluyanov and D. Vanderbilt, Computing topological invariants without inversion symmetry, Phys. Rev. B **83**, 235401 (2011).
[111] H. Hahn and P. Ness, Über Subchalkogenidphasen des Titans, Z. Anorg. Allg. Chem. **302**, 17 (1959).
[112] H. Hahn, B. Harder, U. Mutschke, and P. Ness, Zur Kristallstruktur einiger Verbindungen und Phasen des Systems Zirkon/Schwefel, Z. Anorg. Allg. Chem. **292**, 82 (1957).
[113] H. Wiedemeier and H. Goldman, Mass transport and crystal growth of the mixed ZrS_2-$ZrSe_2$ system, J. Less-Common Met. **116**, 389 (1986).
[114] H. Hahn and P. Ness, Über das System Zirkon/Selen, Z. Anorg. Allg. Chem. **302**, 37 (1959).
[115] I. M. Schewe-Miller, and V. G. Young, Hf_2Se_3, a new structure in the binary Hf-Se system, J. Alloys Compd. **216**, 113 (1994).
[116] H. Sodeck, H. Mikler, and K. L. Komarek, Transition metal-chalcogen systems, VI: The zirconium-tellurium phase diagram, Monatsh Chem. **110**, 1 (1979).
[117] G. Örlygsson and B. Harbrecht, Structure, properties, and bonding of ZrTe (MnP type), a low-symmetry, high-temperature modification of ZrTe (WC type), J. Am. Chem. Soc. **123**, 4168 (2001).
[118] G. Örlygsson and B. Harbrecht, The crystal structure of WC type ZrTe. Advantages in chemical bonding as contrasted to NiAs type ZrTe, Z. für Naturforschung B **54**, 1125 (1999).
[119] See Supplemental Material at http://link.aps.org/supplemental/10.1103/PhysRevB.97.054305 for (1) optimized lattice parameters of MX as compared with available experimental data [111-118], (2) electronic structures of ZrSe, (3) evolution of the electronic structure around the Weyl points (WPs) in ZrSe, (4) surface electronic band structures of (0001) and $(10\bar{1}0)$ surfaces of ZrSe, (5) Fermi surfaces of the (0001) and $(10\bar{1}0)$ surfaces of ZrSe, and (6) DFT-derived phonon dispersions of the nine MX compounds.